AGU PUBLICATIONS

JGR

Journal of Geophysical Research: Space Physics

RESEARCH ARTICLE

10.1002/2013JA019455

Key Points:
- Combined distributions of the ionospheric FAC and convection are shown
- The presence of IMF Bx weakens the signatures produced by IMF Bz
- IMF By can cause dayside reconnection to open closed field lines when IMF Bz>0

Correspondence to:
L. Juusola,
Liisa.Juusola@fmi.fi

Citation:
Juusola, L., S. E. Milan, M. Lester, A. Grocott, and S. M. Imber (2014), Interplanetary magnetic field control of the ionospheric field-aligned current and convection distributions, *J. Geophys. Res. Space Physics*, *119*, 3130–3149, doi:10.1002/2013JA019455.

Received 16 SEP 2013
Accepted 26 MAR 2014
Accepted article online 31 MAR 2014
Published online 16 APR 2014

Interplanetary magnetic field control of the ionospheric field-aligned current and convection distributions

L. Juusola[1], S. E. Milan[2], M. Lester[2], A. Grocott[3], and S. M. Imber[2]

[1]Finnish Meteorological Institute, Helsinki, Finland, [2]Department of Physics and Astronomy, University of Leicester, Leicester, UK, [3]Department of Physics, University of Lancaster, Lancaster, UK

Abstract Patterns of the high-latitude ionospheric convection and field-aligned current (FAC) are a manifestation of the solar wind-magnetosphere-ionosphere coupling. By observing them we can acquire information on magnetopause reconnection, a process through which solar wind energy enters the magnetosphere. We use over 10 years of magnetic field and convection data from the CHAMP satellite and Super Dual Auroral Radar Network radars, respectively, to display combined distributions of the FACs and convection for different interplanetary magnetic field (IMF) orientations and amplitudes. During southward IMF, convection follows the established two-cell pattern with associated Region 1 and Region 2 FACs, indicating subsolar reconnection. During northward IMF, superposed on a weak two-cell pattern there is a reversed two-cell pattern with associated Region 0 and Region 1 FACs on the dayside, indicating lobe reconnection. For dominant IMF B_x, the sign of B_z determines whether lobe or subsolar reconnection signatures will be observed, but B_x will weaken the signatures compared to pure northward or southward IMF. When the IMF rotates from northward to duskward or dawnward, the distinct reversed and forward two-cell patterns start to merge into a distorted two-cell pattern. This is in agreement with the IMF B_y displacing the reconnection location from the open lobe field lines to closed dawn or dusk field lines, even though IMF $B_z > 0$. As the IMF continues to rotate southward, the distorted pattern transforms smoothly to that of the symmetric two-cell pattern. While the IMF direction determines the configuration of the FACs and convection, the IMF amplitude affects their intensity.

1. Introduction

The patterns of high-latitude ionospheric convection and field-aligned current are controlled by the orientation of the interplanetary magnetic field (IMF). Although the IMF magnitude, as well as solar wind speed and density, affects the intensity of the ionospheric distributions, it is the orientation of the IMF that determines the configuration.

Any IMF orientation can produce reconnection at the magnetopause, provided that there is a region where the IMF and Earth's magnetic field are close to antiparallel and that there is sufficient plasma convection toward that region to bring the two fields in contact. When the IMF is southward ($B_z < 0$), reconnection between the IMF and Earth's magnetic field takes place on the dayside around the subsolar point, transferring closed dayside flux to open nightside flux. This produces the well-known two-cell convection pattern in the ionosphere, with antisunward flow across the polar cap and sunward return flow at lower latitudes [*Dungey*, 1961]. When the IMF is northward ($B_z > 0$), reconnection takes place behind the cusps, where the IMF draped over the magnetopause merges with already open tail lobe field lines, not changing the amount of open flux [*Russell*, 1972]. It is also possible for the same IMF field line to reconnect with open tail field lines in both hemispheres, thus transferring open nightside flux to closed dayside flux. The new dayside flux would then return to the nightside along the flanks of the magnetosphere. Such dual lobe reconnection, although rare, has indeed been observed [*Imber et al.*, 2006, 2007]. The ionospheric convection pattern corresponding to northward IMF consists of two reverse cells confined within the polar cap and two normal cells at lower latitudes [*Dungey*, 1963], the latter possibly being caused by a viscous interaction [*Axford and Hines*, 1961] or ongoing nightside reconnection [*Milan*, 2004].

While IMF B_z determines whether magnetopause reconnection takes place on the dayside or nightside of the cusp, IMF B_y produces a dawn-dusk asymmetry at the magnetopause reconnection location [*Luhmann et al.*, 1984], driving a corresponding asymmetry in the ionospheric convection pattern [e.g., *Weimer*, 1995, 1996]. For a given sign of IMF B_y, the asymmetry is reversed in the Northern and in the Southern

Hemispheres. IMF B_x, on the other hand, produces north-south asymmetry in the magnetopause reconnection location. For $B_z < 0$, a positive (negative) B_x might be expected to move the preferred reconnection location northward (southward) along the closed dayside field line. As closed dayside flux would anyway be transferred to open nightside flux, the ionospheric projection would be expected to be similar to that of southward IMF. For $B_z > 0$, a positive (negative) B_x would be expected to favor open-to-open lobe reconnection in the Southern (Northern) Hemisphere. However, as the effect of IMF B_x on the ionospheric convection pattern has received less attention than that of B_z or B_y, the effects have not been fully documented.

The ionospheric convection is linked to ionospheric and magnetic field-aligned electric currents. Statistically, the large-scale field-aligned currents at high latitudes consist of a pair of concentric rings, called Region 1 and Region 2. The poleward Region 1 flows into the ionosphere on the dawnside and out of the ionosphere on the duskside, whereas the equatorward Region 2 has an opposite polarity at a given local time sector [*Iijima and Potemra*, 1976; *Weimer*, 2001; *Papitashvili et al.*, 2002; *Anderson et al.*, 2008]. With increasing activity, the current system intensifies and expands to lower latitudes. For northward IMF, an additional pair of upward (prenoon) and downward (postnoon) field-aligned current forms on the dayside, poleward of the Region 1 currents. This current system is called NBZ or Region 0 [e.g., *Stauning*, 2002]. The more general term Region 0 is used of any current system located poleward of Region 1, including those during strong IMF B_y [e.g., *Weimer*, 2001; *Papitashvili et al.*, 2002; *Anderson et al.*, 2008]. As with the ionospheric convection, the effect of a strong IMF B_x on the current distribution has not been extensively studied.

Although the overall response of both the ionospheric convection and field-aligned current distribution to IMF B_z and B_y has been established, the mutual relationship of the two patterns has not been comprehensively examined. The relationship would, for instance, help us understand the mapping of the field-aligned currents from the ionosphere to the magnetosphere.

In this study, we will examine in detail the effect of IMF B_x, B_y, and B_z on the ionospheric distribution of convection and field-aligned current. Our tools comprise a novel set of models for high-latitude ionospheric currents, parameterized with the IMF direction and amplitude. Although over the years, several such models have been constructed [e.g., *Weimer*, 2001; *Papitashvili et al.*, 2002; *Anderson et al.*, 2008; *He et al.*, 2012], our models differ from these in that not only is the field aligned but also the horizontal ionospheric current distribution resolved. *Juusola et al.* [2009] determined both horizontal and field-aligned current density components but only in the auroral region. Our models will cover the entire high-latitude region poleward of about 50° at the relatively high 2° × 2° resolution. The set of current density models is complemented by a similarly parameterized set of convection models, resolved at the same spatial grid. Reproducing the well-known features of the ionospheric field-aligned current and convection distributions during different combinations of IMF B_z and B_y will also serve as a validation for our new models.

We will start by introducing the data and the models (section 2), then show the IMF B_x, B_y, and B_z dependence of the ionospheric convection and field-aligned current patterns (section 3) and discuss the results and their implications (section 4). Our conclusions are summarized in the final section (section 5).

2. Data and Method

We have used magnetic field measurements from the low-orbit Challenging Minisatellite Payload (CHAMP, http://op.gfz-potsdam.de/champ/) satellite to determine global statistical maps of the horizontal and field-aligned ionospheric electric currents. Super Dual Auroral Radar Network (SuperDARN, http://vt.superdarn.org/) measurements have been used to determine corresponding maps of the ionospheric electric field and convection. All maps were projected onto a 40 × 40 Cartesian grid of cells 222 km × 222 km in size (222 km is equivalent to 2° of latitude), centered on the geomagnetic pole with rows and columns aligned along the noon-midnight and dawn-dusk meridians (Figure 1, blue dots) [*Milan et al.*, 2010].

2.1. Determining the Ionospheric Horizontal and Field-Aligned Current Distribution

The CHAMP satellite measured Earth's magnetic field from 15 July 2000 to 19 September 2010. The satellite had an almost circular, near polar orbit with an initial altitude of 454 km, and orbital period of 1.5 h. All local time sectors were covered in 131 days. Figure 2c shows the satellite's daily minimum, maximum (red color), and mean altitude (black) during the lifetime of the mission. The monthly smoothed sunspot number is shown in gray in the background. The mission spanned the declining phase of solar cycle 23 and the

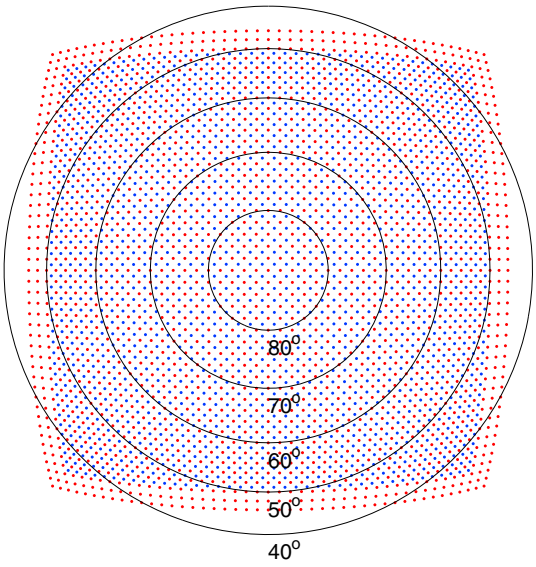

Figure 1. Blue dots: The grid [*Milan et al.*, 2010] onto which all the models have been projected. Red dots: Locations of the 2-D SECS poles. Constant AACGM latitudes are indicated by the circles. MLT midnight is at the bottom, dawn on the right, noon at the top, and dusk on the left.

beginning of cycle 24. We have used the 1 s vector magnetic field data (B_x – positive north, B_y – positive east, B_z – positive down). The Potsdam Magnetic Model of the Earth (POMME) magnetic field model [*Maus et al.*, 2006] was used to subtract the baseline (POMME-4 was used for 2000–2001 and POMME-6 for 2002–2010).

The disturbance magnetic field that remains after the baseline has been subtracted is mainly caused by horizontal and field-aligned ionospheric electric currents. As the horizontal currents are concentrated in a relatively thin layer between about 90 and 130 km altitude [*Kamide et al.*, 1977], they are often modeled as a spherical surface current distribution at 100 km altitude. In order to determine the currents, the locations of CHAMP were first converted from geographic latitude and longitude to Altitude Adjusted Corrected GeoMagnetic (AACGM) latitude [*Baker and Wing*, 1989] and Magnetic Local Time (MLT). B_x and B_y were rotated from geographic to geomagnetic dipole coordinates. The mean and the standard deviation (SD) of B_x, B_y, and B_z were then calculated in each grid cell. The difference between the maximum and minimum satellite altitude was 244 km, which is approximately the size of one horizontal grid cell. Thus, we did not bin the CHAMP data according to altitude, although that would also have been possible. Instead, we used the mean altitude in the cell as the altitude of the grid point.

As an example, Figure 2a displays the number of observations and Figure 2b the mean horizontal (arrows) and vertical (color) magnetic field distribution for the CHAMP data set around 370 km altitude. Data from both hemispheres, projected onto the Northern hemisphere, were used. A Southern Hemisphere data point (latitude, MLT, B_x, B_y, B_z) was projected onto Northern Hemisphere according to (−latitude, MLT, B_x, $-B_y$, and $-B_z$).

The 2-D Spherical Elementary Current System (SECS) method [*Amm*, 1997; *Amm and Viljanen*, 1999] was used to determine the ionospheric and field-aligned current distribution corresponding to the magnetic field distribution. With this technique, the ionospheric current density at 100 km altitude is expressed as a superposition of divergence-free (df) and curl-free (cf) SECSs. The method does not require any assumptions about the latitudinal or longitudinal geometry of the current distribution or the underlying conductivity distribution. The locations of the SECS poles are distributed over the region of interest, and each SECS may have a different amplitude. The magnetic fields of the SECSs can be expressed analytically, which makes it possible to determine the ionospheric current density, i.e., the SECS amplitudes, by optimally matching the measured disturbance magnetic field to the superposed magnetic field of the SECSs.

While only the divergence-free amplitudes can be determined from ground-based magnetic field data [*Fukushima*, 1976; *Untiedt and Baumjohann*, 1993], both the divergence-free and curl-free SECS amplitudes can be determined from low-orbit satellite magnetic field data. In other words, only the so-called equivalent current distribution can be determined from ground magnetic field data, whereas the full horizontal and (radial) field-aligned current distribution can be obtained from low-orbit satellite data, or a combination of both. By an ionospheric and field-aligned current density model we refer to a set of divergence-free and curl-free SECS pole locations (Figure 1, red dots) and amplitudes. The current densities were calculated at the grid points shown in Figure 1 (blue dots).

As an example, the arrows in Figures 2d–2f display the divergence-free component, the curl-free component, and the total horizontal current density, respectively, corresponding to the magnetic field map shown in Figure 2b. The color in Figure 2d shows the curl of the equivalent current density, which is often used as a proxy for the field-aligned current density, and the color in Figures 2e and 2f shows the field-aligned

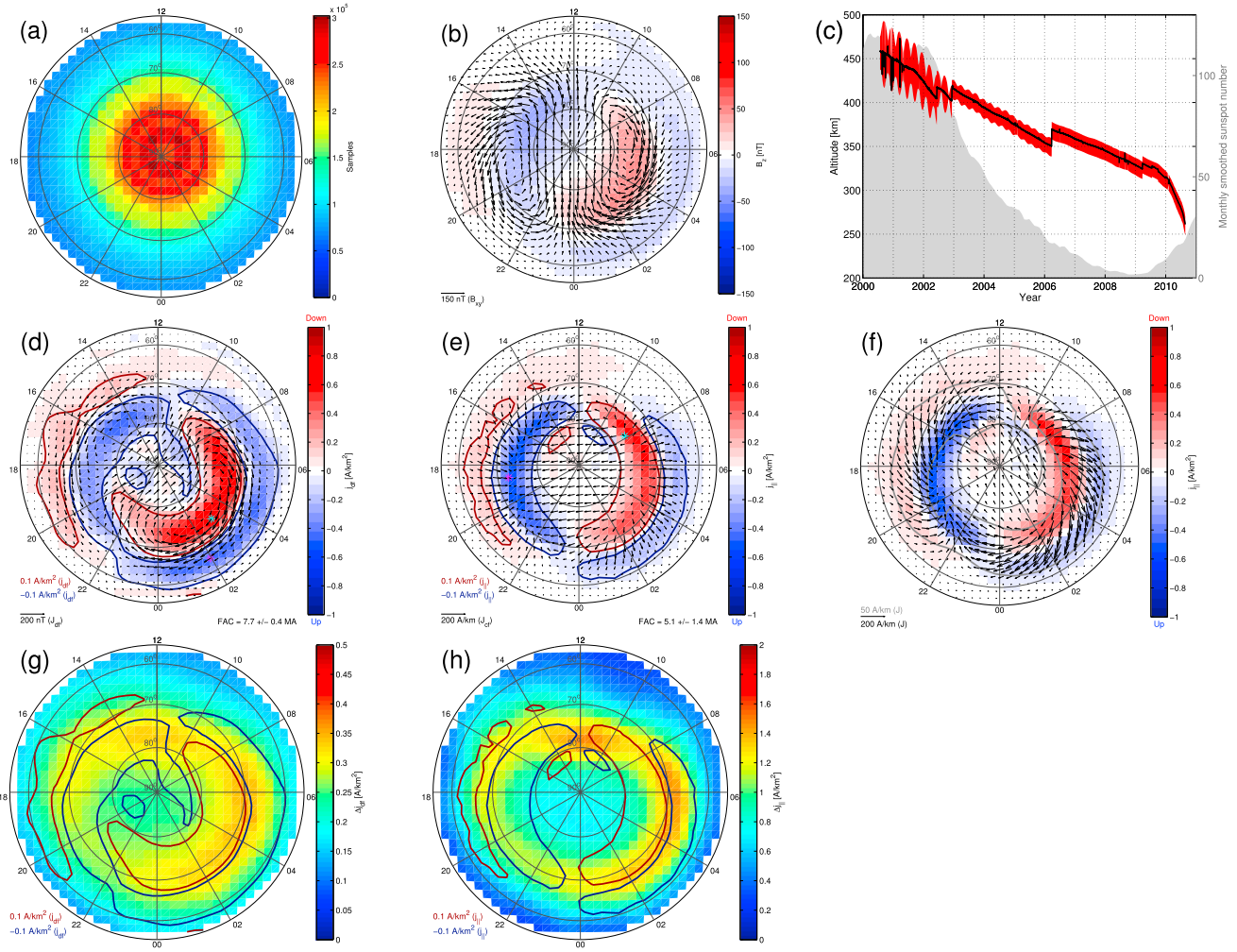

Figure 2. (a) Number of CHAMP magnetic field samples as a function of AACGM latitude and MLT. (b) Mean of the disturbance magnetic field horizontal (arrows) and vertical (color) components measured by CHAMP. (c) Daily minimum, maximum (red color), and mean (black curve) altitude of CHAMP (left axis) and the monthly smoothed sunspot number (gray color, right axis) as a function of time. (d) Mean divergence-free or equivalent component of the horizontal current density (arrows) and curl of the equivalent current density (color) at 100 km altitude. The locations of the minimum and maximum of the curl are indicated by the magenta and cyan asterisk, respectively, and the blue and red curves are the $\pm$0.1 A/km^2 contours. The proxy field-aligned current is given in the bottom right corner. (e) Mean curl-free component of the horizontal current density (arrows) and field-aligned current density (color) at 100 km altitude. The locations of the minimum and maximum of the field-aligned current density are indicated by the magenta and cyan asterisk, respectively, and the blue and red curves are the $\pm$0.1 A/km^2 contours. The field-aligned current is given in the bottom right corner. (f) Horizontal current density (arrows) and field-aligned current density (color) at 100 km altitude. The gray curve is the 50 A/km contour. (g) Uncertainty of the curl of the equivalent current density. The contours are from Figure 2d. (h) Uncertainty of the field-aligned current density. The contours are from Figure 2e. The distributions in Figures 2d–2f were determined from the mean magnetic field in Figure 2b, and the distributions in Figures 2g and 2h from the SD of the magnetic field (not shown).

current density. The locations of the minimum and maximum of the curl and field-aligned current density are indicated by the magenta and cyan asterisks, respectively, and the blue and red curves are the $\pm$0.1 A/km^2 contours. The gray curve in Figure 2f marks the region inside of which there are significant horizontal currents. Figures 2g and 2h show the uncertainty of the curl of the equivalent current density and field-aligned current density, respectively, estimated from the SD of the magnetic field (ΔB_x,ΔB_y,ΔB_z, not shown) using the propagation of error. The contours from Figures 2d and 2e are shown for reference. Note that the color scales in Figures 2g and 2h are different from Figures 2d and 2e. The numbers in the bottom right corner of Figures 2d and 2e give the proxy field-aligned current and the field-aligned current, respectively. The field-aligned current was calculated as a sum of the absolute value of the field-aligned current density in each grid cell times the area of the grid cell over the grid shown in Figure 1 (blue dots). The

uncertainty of the field-aligned current was estimated from the uncertainty of the field-aligned current density using the propagation of error.

The assumption of radial field lines is the best at latitudes near the magnetic poles and becomes worse toward the equator. Our maps extend from 90° to 55° latitude. Compared to a dipole field line, mapping along a radial field line from 400 km altitude to 100 km altitude at 55° latitude will shift the footpoint

$$\arccos\left(\sqrt{\frac{R_E + 100\ \text{km}}{R_E + 400\ \text{km}}}\cos(55°)\right) - 55° = 0.89° \tag{1}$$

equatorward (1 R_E = 6370 km). At 45° latitude the shift would be 1.3°, which is still less than the resolution of our models. At 55° latitude, the dipole magnetic field deviates

$$\arccos\left(\frac{2\sin(55°)}{\sqrt{1+3\sin^2(55°)}}\right) = 19° \tag{2}$$

from the radial direction, and at 45° latitude the deviation is 27°. The geometry of the field lines affects the magnetic field produced by the field-aligned currents. Estimating the effect on the resulting current distributions would be complicated in the general case. However, in case the current distribution can be estimated not to vary in the longitudinal direction (e.g., the current systems in the dawn and dusk sectors of the auroral oval), B_x and B_z would be produced by the divergence-free horizontal current density J_y and would not be affected by the radial or dipole geometry of the field lines. B_y would be produced by the curl-free horizontal current density J_x and the field-aligned current density. The B_y produced by a J_x together with a dipole sheet current would be only slightly weaker,

$$\sqrt{\frac{R_E + 100\ \text{km}}{R_E + 400\ \text{km}}} = 0.98 \tag{3}$$

times the B_y produced by the same J_x together with a radial sheet current of the same amplitude [*Juusola et al.*, 2006].

2.2. Determining the Ionospheric Convection Map

The SuperDARN radar network assimilates Doppler shift measurements of HF radio waves backscattered from the *F* region ionosphere to determine the $\mathbf{E} \times \mathbf{B}$ flow patterns in the northern and southern polar regions (poleward of approximately 50° latitude) [*Greenwald et al.*, 1995; *Chisham et al.*, 2007]. The electric field can be represented as an electrostatic potential pattern. Where radar measurements are insufficient to determine the electrostatic potential, they are supplemented by additional points taken from an empirical model of the convection pattern parameterized by the IMF orientation and strength [*Ruohoniemi and Baker*, 1998].

We have used a SuperDARN data set, which comprises the electrostatic potential patterns in a magnetic latitude and local time coordinate system at a cadence of 120 s from 2000 to 2010, projected onto the grid described above. The data set includes information on the grid cells with observations within them. To avoid parts of the potential constrained only by the statistical model, we have only utilized cells with actual observations in them. Furthermore, we have only included maps that can be considered reliable, that is, maps that contain at least 200 vectors and have a steady lower latitude boundary (known as the Heppner-Maynard boundary).

In order to obtain a statistical ionospheric convection map comparable with the statistical current distributions, the mean and the SD of the electrostatic potential Φ were computed for each grid cell. The 2-D SECS basis functions were then used to calculate the electric field at 100 km altitude, assuming that the (radial) background magnetic field lines are equipotentials. The corresponding convection pattern was obtained as $\mathbf{V} = \mathbf{E} \times \mathbf{B}/B^2$.

As an example, Figure 3a shows the number of observations, Figure 3b the mean electrostatic potential (color) and electric field (arrows). The locations of the minimum and maximum of the electrostatic potential are indicated by the magenta and cyan asterisk, respectively, and the blue and red curves are the ±5 kV contours. Figure 3c shows the field-aligned current distribution (color) from Figure 2f as well as the

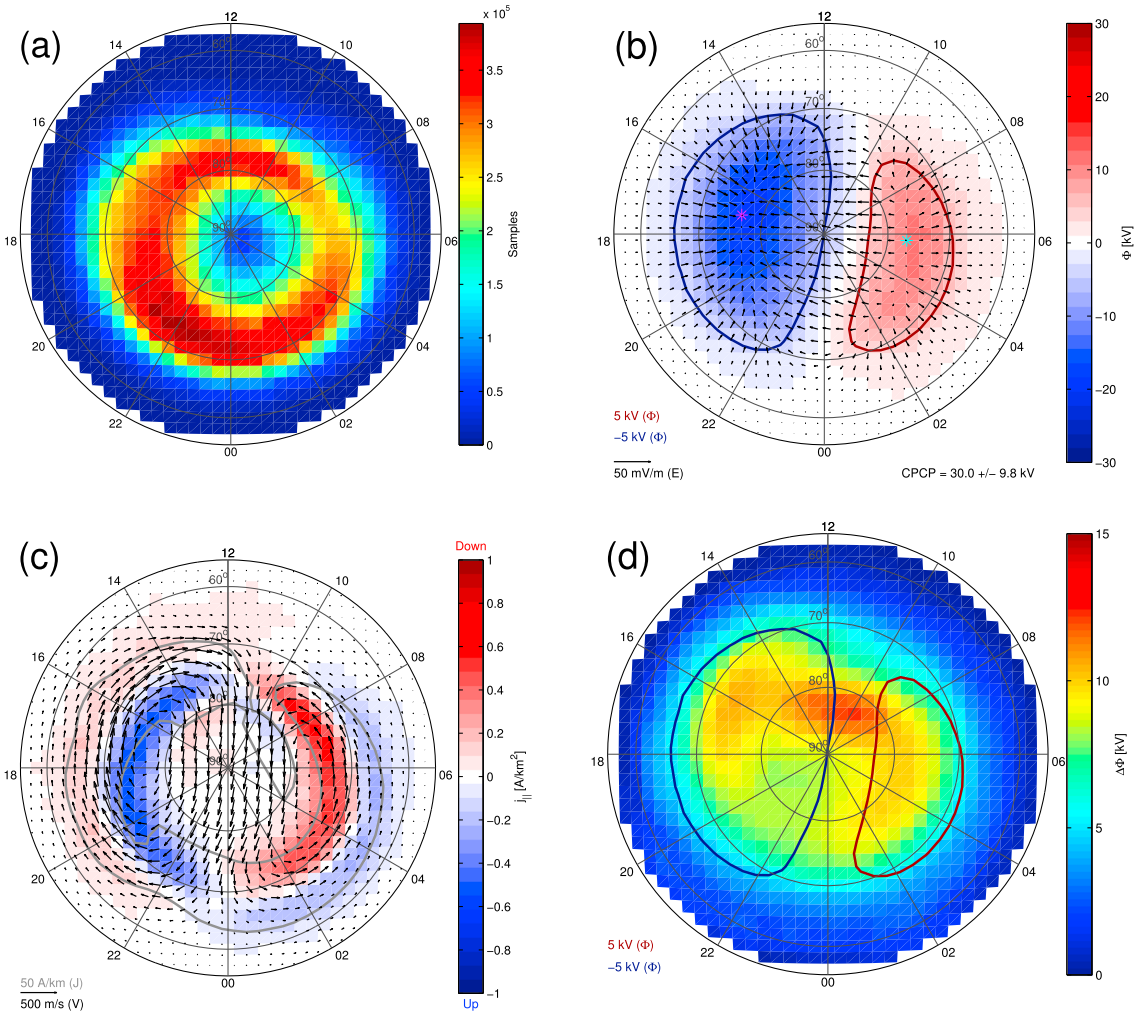

Figure 3. (a) Number of SuperDARN map potential samples as a function of AACGM latitude and MLT. (b) Mean electrostatic potential (color) and electric field at 100 km altitude (arrows) determined from SuperDARN measurements. The locations of the minimum and maximum of the electrostatic potential are indicated by the magenta and cyan asterisks, respectively, and the blue and red curves are the ±5 kV contours. The cross-polar cap potential (CPCP) is given in the bottom right corner. (c) Field-aligned current density from Figure 2f (color) and the mean convection velocity at 100 km altitude (arrows) determined from the electric field distribution in Figure 3b. The gray curve is from Figure 2f. (d) SD of the electrostatic potential. The contours are from Figure 3b.

convection velocity (arrows). The gray curve is the same as in Figure 2f. SuperDARN data from both hemispheres, projected onto the Northern Hemisphere, were used. A Southern Hemisphere data point (latitude, MLT, Φ) was projected onto northern hemisphere according to: (−latitude, MLT, Φ). Figure 3d shows the SD of the electrostatic potential. The contours from Figure 3b are shown for reference. Note that the color scales for Figures 3b and 3d are not the same. The cross-polar cap potential (CPCP), i.e., the difference between the maximum and minimum of the electrostatic potential in the grid of Figure 1 (blue dots), is given in the bottom right corner of Figure 3b. The uncertainty of the CPCP (ΔCPCP) was estimated from the SD of the electrostatic potential (ΔΦ) as $\Delta CPCP = (\Delta CPCP_- + \Delta CPCP_+)/2$, where $\Delta CPCP_- = |\min(\Phi - \Delta\Phi) - \min(\Phi)|$ and $\Delta CPCP_+ = \max(\Phi + \Delta\Phi) - \max(\Phi)$.

2.3. Parameterization of the Models

In order to create maps for different IMF conditions, solar wind data at 1 min resolution, propagated to Earth's bow shock nose, were extracted from NASA/Goddard Space Flight Center's (GSFC's) OMNI data set through the OMNIWeb interface (http://omniweb.gsfc.nasa.gov/). The OMNIWeb data were further delayed by 15 min in order to take into account the signal transit time from the magnetopause to the CHAMP altitude [*Weimer et al.*, 2003]. Any occurrences of the prescribed parameterization condition within 15 min of each other were combined together, regardless of any data points in between that did not

meet the condition. For the IMF data, we have used Cartesian (x, y, z) Geocentric Solar Magnetospheric (GSM) coordinates.

When combining CHAMP magnetic field measurements or SuperDARN electrostatic potentials from the Northern and Southern Hemisphere, the IMF direction was taken into account such that data from the Northern Hemisphere obtained when IMF $B_y < 0$ were combined with data from the Southern Hemisphere obtained when IMF $B_y > 0$, and data from the Northern Hemisphere obtained when IMF $B_x < 0$ were combined with data from the Southern Hemisphere obtained when IMF $B_x > 0$.

3. Observations

3.1. General Distributions

Figure 2d (arrows) shows the divergence-free or equivalent current density ($\mathbf{J}_{df}$), that is, the distribution that produces the magnetic field signatures observed on ground. No binning according to IMF has been applied to the general distributions in Figures 2 and 3. As expected, the pattern in Figure 2d consists of the eastward electrojet on the duskside auroral oval and the westward electrojet on the nightside and on the dawnside. The amplitude of the westward current is clearly stronger than that of the eastward current, and the region of enhanced westward current intrudes far to the duskside poleward of the eastward electrojet, forming a pattern typical for the Harang discontinuity region. In the polar cap, the equivalent current is directed sunward and dawnward.

Figure 2e (arrows) shows the curl-free current density ($\mathbf{J}_{cf}$) and the field-aligned current density (color). This part of the ionospheric current system is invisible on the ground. The field-aligned current forms the poleward ring of Region 1 and the equatorward ring of Region 2. The nightside and dayside changes of polarity for Region 1 and Region 2 do not take place in the same local time sectors. On the nightside, Region 1 changes polarity at midnight, whereas for Region 2 this happens in the premidnight region, around 22 MLT. On the dayside, Region 1 changes polarity just before noon, whereas for Region 2 this happens earlier, around 10 MLT. Both Region 1 and Region 2 form distinct rings at all MLT sectors. In the premidnight region, there is no sign of a three-sheet structure formed by overlapping sheets of downward Region 1, upward Region 1 merging with upward Region 2, and downward Region 2 [*Iijima and Potemra*, 1976].

Figure 2d (color) shows the curl of the equivalent current density. If the Hall and Pedersen conductance only had gradients in the direction of the electric field, the curl would be proportional to the field-aligned current density. Comparison with the actual field-aligned current distribution in Figure 2e reveals that, at least statistically, this is a fairly good assumption outside of the midnight and noon sectors. Especially in the premidnight sector, the curl produces the three-sheet structure not present in the field-aligned current distribution. On the dayside, the curl indicates upward Region 2 field-aligned current where the real current is downward. The minimum and maximum of the field-aligned current density, indicated by the magenta and cyan asterisks in Figure 2e, are related to the Region 1 current system, with the maximum on the dayside and minimum at dusk. The minimum and maximum of the curl of the equivalent current density, on the other hand, are located in the postmidnight sector, where the equivalent current density is strongest.

Besides the curl of the equivalent density, another often used proxy for the field-aligned current density is the vorticity of the ionospheric plasma flow, a quantity that can be determined from SuperDARN measurements. In the limit of uniform ionospheric conductances, the vorticity will become proportional to the field-aligned current density. Our results about the curl of the equivalent current density are in agreement with those of *Chisham et al.* [2009], who showed that in an average sense, vorticity is a good proxy for field-aligned currents.

Figure 2f (arrows) shows the total horizontal current system, that is, $\mathbf{J}_{df} + \mathbf{J}_{cf}$. On the dawnside, the region of enhanced horizontal current (marked in Figure 2f, gray curve) encompasses the majority of both Region 1 and Region 2 current, whereas on the duskside, the region of horizontal current narrows down toward later MLTs, such that a significant part of the upward Region 1 current is left poleward of the horizontal current region. On the nightside, the horizontal current is mainly westward and forms a bulge. At the poleward part of this bulge, there is downward Region 1 current in the east and upward current in the west. At the equatorward part of the bulge, the Region 2 current is upward. On the dayside, there is a gap in the region of enhanced horizontal current.

Because our models are based on mean values, they are likely to produce weak values in regions where there are high levels of either temporal or spatial (scale sizes smaller than the 2° resolution of our distributions) fluctuations. Figure 2h displays the uncertainty of the field-aligned current density. The highest uncertainty can be found between the large-scale structures, i.e., between the Region 1 and Region 2 sheets in the latitudinal direction, particularly on the dawnside, but also between the duskside and dawnside Region 1 sheets in the MLT direction, particularly on the dayside. This could be related not only to slightly different locations of the large-scale structures during different IMF conditions but also to structures that are smaller in size than the 2° grid cells. *Ritter et al.* [2004] have reported that the transition from the downward Region 1 to upward Region 2 on the dawnside occurs above the westward auroral electrojet and is characterized by alternating upward and downward field-aligned currents. Consequently, they found the most intense upward field-aligned currents not in the Region 2 proper but above the auroral electrojet and suggested that these probably give rise to a high conductivity, a requirement for the intense electrojet current.

Figure 2g shows the uncertainty of the curl of the equivalent current density. These values are clearly smaller than those related to the field-aligned current density (note that the color scales are different for Figures 2g and 2h). The curl of the equivalent current density represents the amplitudes of the divergence-free SECSs in the same way the field-aligned current density represents the amplitudes of the curl-free SECSs (the SECS amplitude divided by the area of the grid cell). The curl-free horizontal current density component closes via field-aligned currents and is, thus, directly connected to the CHAMP altitude. The divergence-free component of the horizontal current density, on the other hand, closes within the ionosphere, i.e., the spherical surface at 100 km altitude, on average 270 km below CHAMP.

The electric field (arrows) and potential (color) in Figure 3b and the convection (arrows) in Figure 3c correspond to the expected two-cell pattern with antisunward flow in the polar cap and sunward return flow at lower latitudes. At dawn and dusk, the antisunward flow is mainly confined poleward of Region 1 and the return flow in the same latitude range as Region 1 and Region 2. The strongest return flows take place near the poleward edge of this region. Particularly in the midnight sector where Region 2 is upward, the statistical flows tend to be relatively weak. Of course, this does not necessarily mean that there are no strong flows in this region, merely that, on average, the flows cancel each other out. However, the level of fluctuations is not particularly large in this region, as shown by the SD of the electrostatic potential in Figure 3d. The highest uncertainty can be found on the dayside, especially between the two convection cells where the mean electrostatic potential is almost zero. This is most likely caused by the combination of data obtained during different IMF orientation (section 3.2).

On the nightside, the antisunward convection in Figure 3c turns slightly duskward. Nonetheless, the most equatorward point where the flow splits dawnward and duskward is located close to midnight, in the same MLT sector where Region 1 changes polarity. This point would be expected to map to the plasma sheet region where earthward flows intrude closest to Earth. The most poleward points where the flows start to turn duskward and dawnward are located at ~18 MLT and ~03 MLT, respectively. In the premidnight MLT sector where the antisunward flow turns duskward, Region 1 is upward, and in the postmidnight sector where the flow turns dawnward, Region 1 is downward. On the dayside, the convergence of the flows from the dawnside and duskside takes place in the same region where there is a gap in the region of enhanced horizontal currents.

Figure 4 shows the sunward component of the convection velocity (V, black curve, left axis) and of the equivalent current density (J_{eq}, red curve, left axis), field-aligned current density ($j_{||}$, blue curve, right axis), and curl of the equivalent current density (j_{eq}, green curve, right axis) as a function of magnetic colatitude at the dawn-dusk meridian (18 MLT corresponds to negative values of colatitude and 06 MLT to positive values). The colatitude ranges of Region 2 (R2) and Region 1 (R1), as determined from the field-aligned current curve, are indicated, and those of Region 1 are highlighted with a cyan shading.

The convection velocity shows two positive peaks that correspond to the sunward return flow, with the amplitude of the duskside peak clearly stronger than that of the dawnside peak. Both the Region 1 and 2 currents are located in the region where the convection velocity changes; Region 1 in the latitude ranges where the velocity changes from the peak sunward values to the peak antisunward value, and Region 2 in the lower latitude ranges where the peak sunward values decreases toward zero. Between the dawnside and

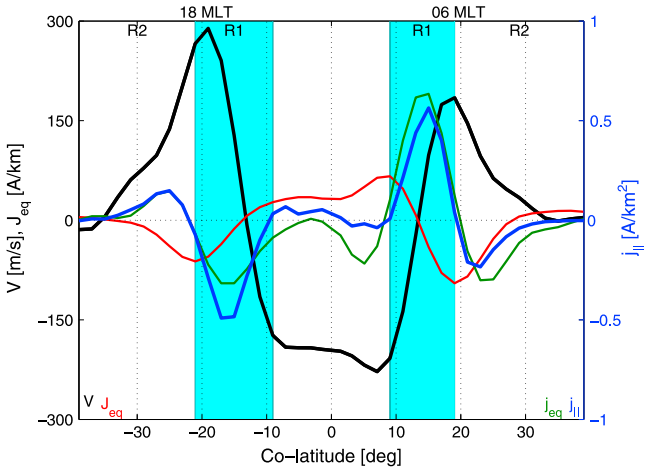

Figure 4. Sunward component of the convection velocity (V, black curve, left axis) and of the equivalent current density (J_{eq}, red curve, left axis), field-aligned current density ($j_{||}$, blue curve, right axis), and curl of the equivalent current density (j_{eq}, green curve, right axis) as a function of AACGM colatitude at the dawn-dusk meridian (18 MLT corresponds to negative values of colatitude and 06 MLT to positive values). The colatitude ranges of Region 2 (R2) and Region 1 (R1), as determined from the field-aligned current curve, are indicated, and those of Region 1 are highlighted with a cyan shading.

duskside Region 1, the antisunward convection velocity remains fairly constant and the field-aligned current is weak.

The equivalent current density can be used as a proxy for the convection velocity under the same assumption as the curl of the equivalent current density can be used for the field-aligned current density. Figure 4 shows that the peaks and sign changes of the equivalent current density coincide with those of the convection velocity. However, opposite to the velocity, for the equivalent current density the dawnside peak is stronger than the duskside peak. The peaks and sign changes of the curl of the equivalent current density agree fairly well with those of the field-aligned current density. What is even more surprising is how well the amplitudes of the two curves match.

3.2. IMF Dependence

Figures 5–8 show the statistical convection pattern determined from SuperDARN data (arrows) and the field-aligned current distribution determined from CHAMP data (color) for different IMF orientations and amplitudes, as specified in Table 1.

From left to right, the columns in Figures 5 and 6 correspond to $B_y < 0$, $B_x > 0$, $B_y > 0$, and $B_x < 0$, respectively, except for the top row of Figure 5, which corresponds to purely northward IMF orientation (the same plot repeated 4 times), and the bottom row of Figure 6 (again the same plot repeated 4 times), which corresponds to purely southward IMF orientation. From top to bottom, the rows in Figure 5 correspond to a decreasing northward IMF component, and the rows in Figure 6 to an increasing southward IMF component. For the two topmost rows in Figure 5, and for the two bottom rows in Figure 6, IMF B_z is the dominant component. For the middle rows, the amplitudes of B_z and B_x or B_y are approximately equal. For the two bottom rows in Figure 5, and for the two topmost rows in Figure 6, either B_x or B_y is the dominant component. For easier comparison, the bottom row of Figure 5 and the top row Figure 6, corresponding to IMF $B_z \approx 0$, are the same. Figures 5 and 6 and Figures 7 and 8 are otherwise the same, except for the IMF amplitude, which is ≤ 5 nT for Figures 5 and 6, and > 5 nT for Figures 7 and 8.

The distributions in Figures 5–8 show that both the Region 1 and Region 2 current systems as well as the two-cell convection pattern exist for all IMF orientations, although their strength increases and they widen and expand to lower latitudes as the IMF rotates from northward to southward. On the nightside, the most equatorward point where the antisunward flow splits toward dawn and dusk is located in the same MLT sector where Region 1 changes polarity.

For pure northward IMF (Figures 5a and 7a), the strongest field-aligned currents are on the dayside. They comprise Region 0 at higher latitudes and enhanced Region 1 at lower latitudes. The associated convection

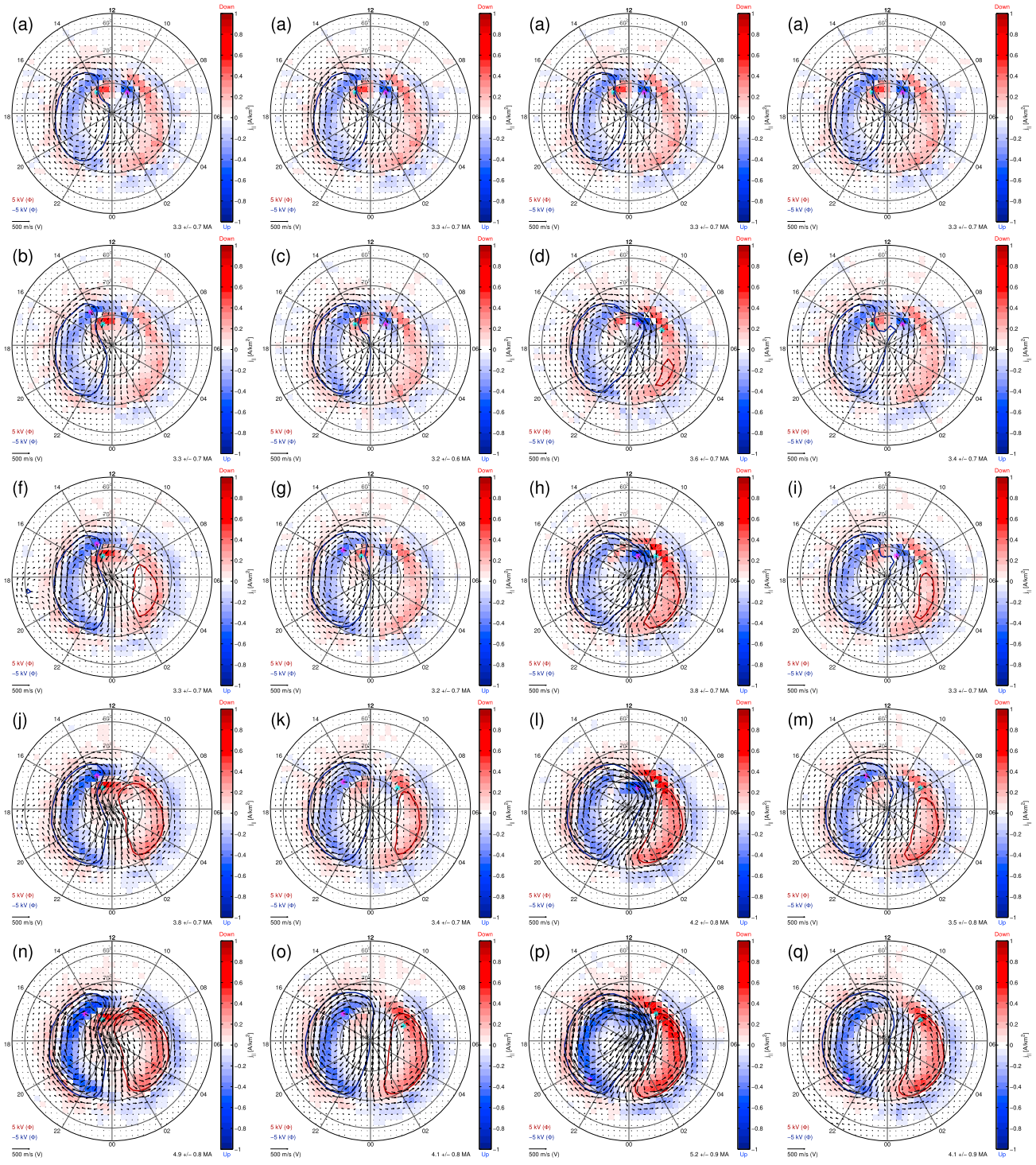

Figure 5. (a–q) Ionospheric field-aligned current density (color) and convection velocity (arrows) at 100 km altitude for different IMF orientations as specified in Table 1, with IMF $B \leq 5$ nT, as a function of AACGM latitude and MLT. The blue and red curves are the ±5 kV contours for the electrostatic potential. The minimum and maximum field-aligned current density are indicated with the magenta and cyan asterisks, respectively, and the absolute value of the field-aligned current is given in the bottom right corner.

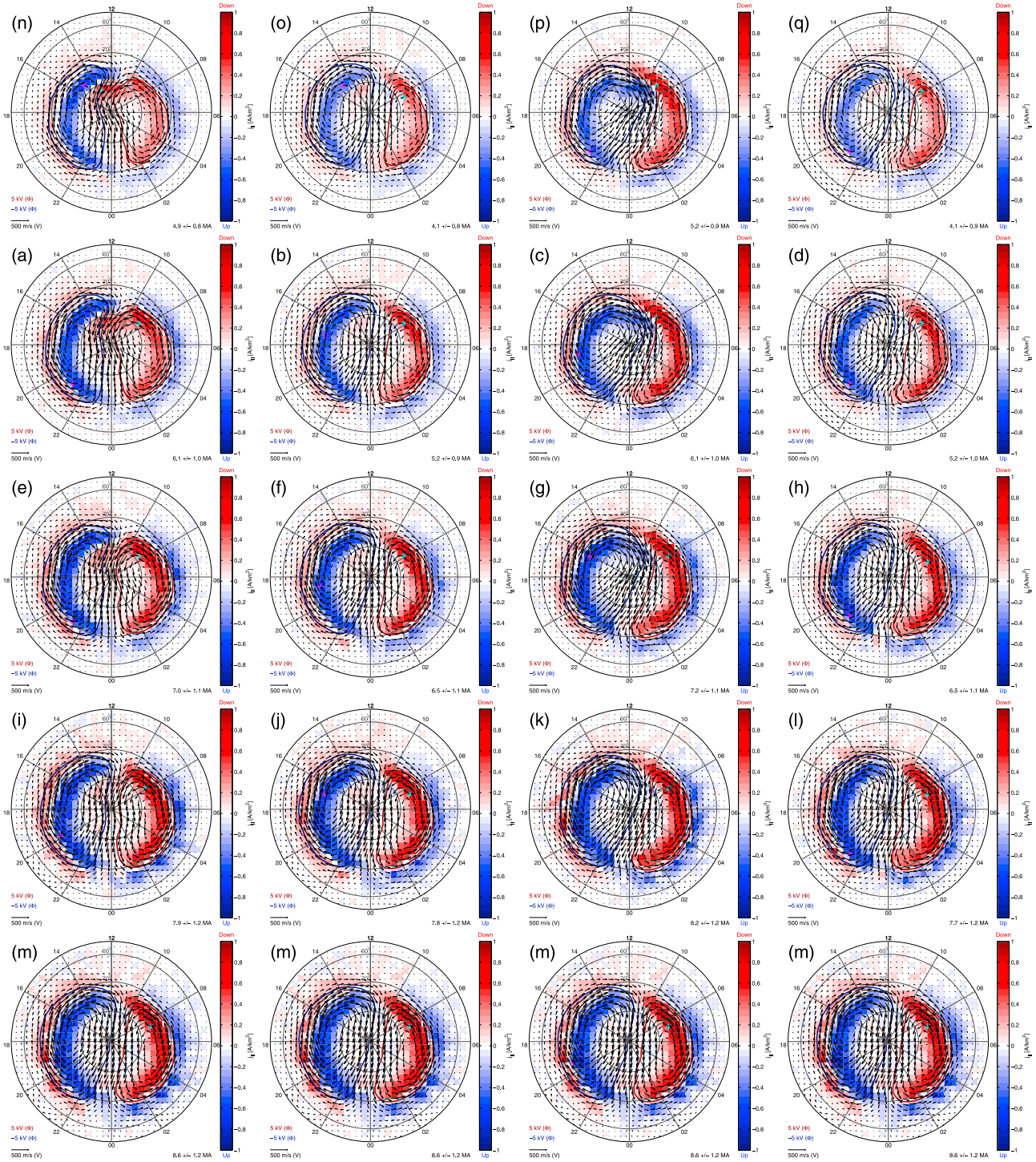

Figure 6. Figure 5 continued.

consists of sunward flow between the pair of upward and downward Region 0 currents and antisunward return flow at lower latitudes between Region 0 and enhanced Region 1 currents. This reversed two-cell convection pattern, which is consistent with lobe reconnection, is superposed on a weak two-cell convection pattern. Although the basic pattern remains the same, a weaker amplitude of the IMF produces weaker amplitudes for both the field-aligned currents and convection. The sunward convection, in particular, is much more clear for IMF $B > 5$ nT (Figure 7a) than for IMF $B \leq 5$ nT (Figure 5a).

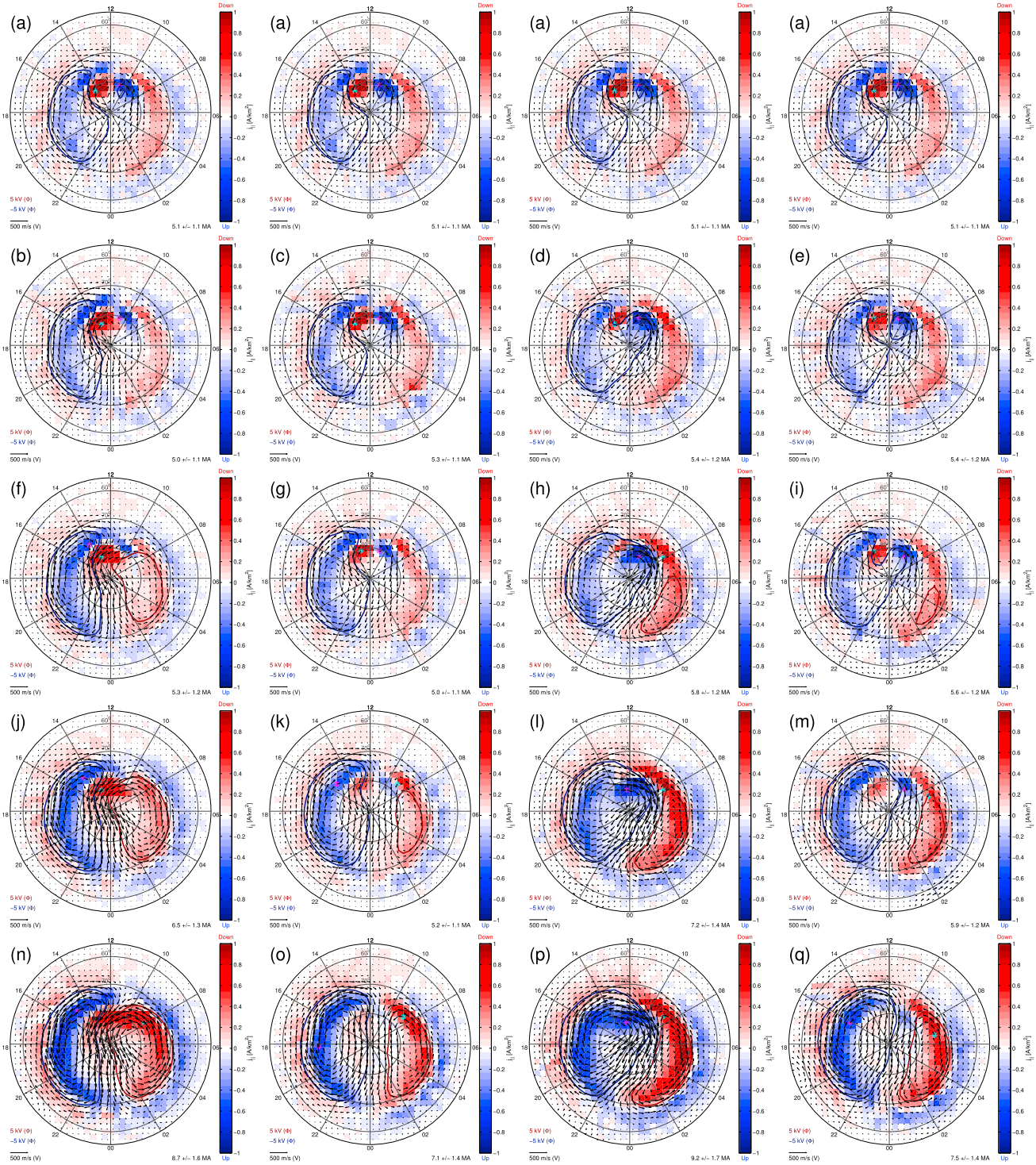

Figure 7. The same as Figure 5 except for IMF $B > 5$ nT instead of IMF $B \leq 5$ nT.

While B_z remains the dominant component, a nonzero B_x (Figures 5c, 5e, 7c, and 7e) does not produce noticeable changes in the pattern. A negative B_y (Figures 5b and 7b), on the other hand, will rotate both the convection and field-aligned current patterns anticlockwise, in agreement with a dawnward shift of the (Northern Hemisphere) lobe reconnection location, and vise versa for a positive B_y (Figures 5d and 7d). The reconnection site remains in the lobe, as both the associated field-aligned current and convection patterns are clearly superposed on a weak two-cell convection pattern and Region 1 and Region 2 field-aligned currents.

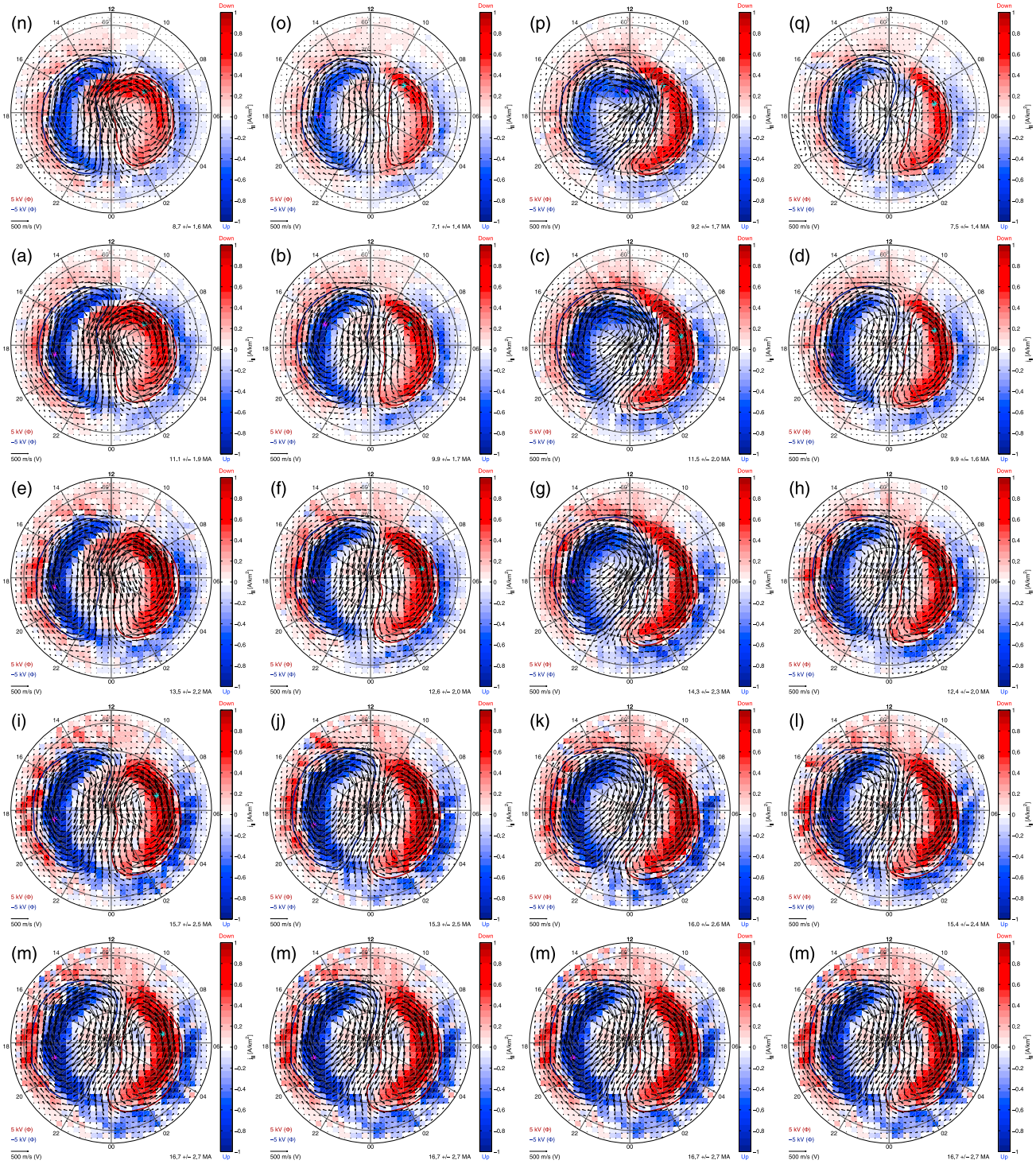

Figure 8. Figure 7 continued.

Milan et al. [2000] showed dayside auroral emissions in the Northern Hemisphere during an interval when IMF B_z was predominantly positive. The emissions consisted of two parts: a postnoon emission at lower latitudes that could correspond to the upward Region 1 in our plots, and an emission at higher latitudes that could correspond to the upward Region 0 in our plots. For IMF $B_y < 0$, this higher-latitude emission was located in the prenoon sector, and for IMF $B_y > 0$, in the postnoon sector. The behavior of the upward

Table 1. IMF Angles $\theta = \arctan(B_z/\sqrt{B_x^2 + B_y^2})$ and $\phi = \arctan(B_y/B_x)$ for the Different Panels in Figures 5–8[a]

			$\phi = -90°$	$\phi = 0°$	$\phi = 90°$	$\phi = 180°$
		Any ϕ	$B_y < 0$	$B_x > 0$	$B_y > 0$	$B_x < 0$
$\theta = 0°$	$(B_z > 0), B \le 5$ nT	5a				
$\theta = 22.5°$	$(B_z > 0), B \le 5$ nT		5b	5c	5d	5e
$\theta = 45°$	$(B_z > 0), B \le 5$ nT		5f	5g	5h	5i
$\theta = 67.5°$	$(B_z > 0), B \le 5$ nT		5j	5k	5l	5m
$\theta = 90°$	$(B_z \approx 0), B \le 5$ nT		5n, 6n	5o, 6o	5p, 6p	5q, 6q
$\theta = 112.5°$	$(B_z < 0), B \le 5$ nT		6a	6b	6c	6d
$\theta = 135°$	$(B_z < 0), B \le 5$ nT		6e	6f	6g	6h
$\theta = 157.5°$	$(B_z < 0), B \le 5$ nT		6i	6j	6k	6l
$\theta = 180°$	$(B_z < 0), B \le 5$ nT	6m				
$\theta = 0°$	$(B_z > 0), B > 5$ nT	7a				
$\theta = 22.5°$	$(B_z > 0), B > 5$ nT		7b	7c	7d	7e
$\theta = 45°$	$(B_z > 0), B > 5$ nT		7f	7g	7h	7i
$\theta = 67.5°$	$(B_z > 0), B > 5$ nT		7j	7k	7l	7m
$\theta = 90°$	$(B_z \approx 0), B > 5$ nT		7n, 8n	7o, 8o	7p, 8p	7q, 8q
$\theta = 112.5°$	$(B_z < 0), B > 5$ nT		8a	8b	8c	8d
$\theta = 135°$	$(B_z < 0), B > 5$ nT		8e	8f	8g	8h
$\theta = 157.5°$	$(B_z < 0), B > 5$ nT		8i	8j	8k	8l
$\theta = 180°$	$(B_z < 0), B > 5$ nT	8m				

[a]The actual data used to construct each panel includes ±22.5° around the given direction.

Region 0 current in our plots is in agreement with this, showing a substantial part of the statistical current in the postnoon sector for $B_y > 0$ and all of it confined to the prenoon sector for $B_y < 0$.

When the magnitude of B_x becomes comparable to (Figures 5g, 5i, 7g, and 7i) or stronger than B_z (Figures 5k, 5m, 7k, and 7m), the lobe reconnection signatures, although still present, clearly weaken. For purely radial IMF (Figures 5o, 5q, 7o, and 7q), very weak signatures of lobe reconnection are still present, but the slight enhancement of the two-cell pattern indicates that some subsolar reconnection is also present in the data set.

As B_y enhances compared to the positive B_z (Figures 5f, 5h, 5j, 5l, 5n, 5p, 7f, 7h, 7j, 7l, 7n, and 7p), Region 0 starts to merge with Region 1, and the reversed two-cell pattern with the regular two-cell pattern. This is consistent with the Northern Hemisphere magnetopause reconnection site moving from nightside toward the dusk flank for $B_y < 0$ (and vise versa for $B_y > 0$). As the reconnection site moves further and further toward the dayside, instead of transferring open nightside field lines to open dayside field lines, it starts to transfer closed duskside field lines to open dawnside field lines. This process is basically similar to subsolar reconnection during negative B_z, and thus, the ionospheric signatures would no longer be expected to form the distinct lobe reconnection pattern but to be those of a distorted subsolar reconnection. The overall enhancement of the two-cell convection pattern and the Region 1 and Region 2 current systems also indicates that open flux is being added to the system even though B_z is not negative.

As IMF B_z turns more and more southward, all signs of lobe reconnection for nonzero B_x (Figures 6b, 6d, 6f, 6h, 6j, 6l, 8b, 8d, 8f, 8h, 8j, and 8l) disappear. The two-cell pattern and the Region 1 and Region 2 current systems amplify, indicating that open flux is being added to the system. The two-cell pattern shows relatively little dawn-dusk asymmetry, indicating that subsolar reconnection takes place symmetrically around the subsolar point.

As IMF B_z turns more and more southward, thus moving the magnetopause reconnection site toward the subsolar region, the dawn-dusk asymmetry in the ionospheric field-aligned current and convection pattern due to B_y weakens (Figures 6a, 6c, 6e, 6g, 6i, 6k, 8a, 8c, 8e, 8g, 8i, and 8k). For purely southward IMF (Figures 6m and 8m), the Region 0 current system does not exist, and the convection follows the relatively dawn-dusk symmetric two-cell configuration.

Although the IMF direction determines the configuration of the field-aligned current density and convection, the IMF amplitude affects their intensity such that a weaker IMF produces weaker field-aligned currents

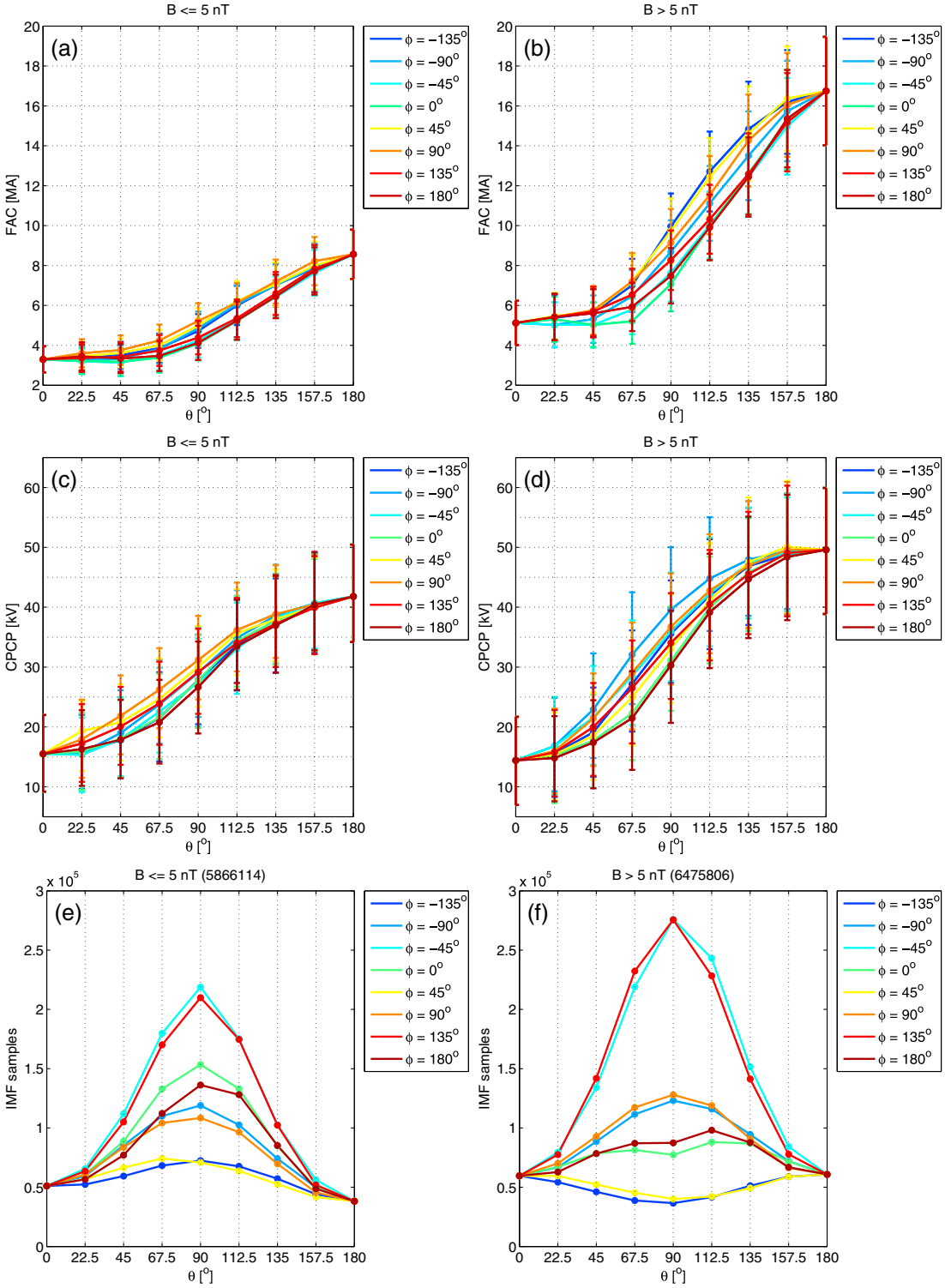

Figure 9. (a) Absolute value of the field-aligned current (defined in section 2.1) in the Northern Hemisphere as a function of the IMF angle $\theta = \arctan\left(B_z/\sqrt{B_x^2+B_y^2}\right)$ for IMF $B \leq 5$ nT. Each curve corresponds to a different value of the IMF angle $\phi = \arctan(B_y/B_x)$. (b) Field-aligned current for IMF $B > 5$ nT. (c) Cross-polar cap potential (CPCP) for IMF $B \leq 5$ nT. (d) CPCP for IMF $B > 5$ nT. (e) Number of IMF samples for $B \leq 5$ nT. The total number of all IMF samples with $B \leq 5$ nT is indicated at the top. (f) Number of IMF samples for $B > 5$ nT.

and flows (Figure 6), and a stronger IMF produces stronger current and flows (Figure 8). Furthermore, for a stronger IMF, the Region 1 and Region 2 current sheets tend to be wider and both their poleward and equatorward edges tend to be located at lower latitudes than for a weaker IMF.

Figures 9a and 9b show the absolute value of the field-aligned current (defined in section 2.1) in the Northern Hemisphere as IMF B_z rotates from northward to southward (elevation angle $\theta = \arctan\left(B_z/\sqrt{B_x^2 + B_y^2}\right)$ increases from 0° to 180°). Each color corresponds to a different value of the IMF angle $\phi = \arctan(B_y/B_x)$. The error bars are derived from the SD of the CHAMP magnetic field using the propagation of error. Although this measure of uncertainty helps in estimating the goodness of the model parameterization (a good parameterization will produce a low level of fluctuations in each grid cell), it does not provide information on the level of fluctuations between neighboring cells. As an example, if there was only one data point in each grid cell, the SD would be zero, but the resulting field-aligned current distribution could still be noisy. A smooth distribution requires a sufficient number of data points in each grid cell. To illustrate the relative numbers of data points in each distribution (as well as how commonly each condition occurs), Figures 9e and 9f show the number of IMF samples in each category. $\phi = -90°$, 0°, 90°, and 180° each correspond to a column in Figures 5–8. There are more or less equal numbers of IMF samples for each of these four ϕ values for a given value of θ. Of the intermediate IMF orientations with about equally strong B_x and B_y components (not shown in Figures 5–8), $\phi = -45°$ or 135° indicates a Parker spiral-like orientation with the highest number of samples, whereas the perpendicular orientation with $\phi = -135°$ or 45° is a rarer occurrence.

For a dominant B_x ($\phi = 0°$ or 180°), the field-aligned current remains weak and fairly constant while $\theta < 90°$. A clear increase of the field-aligned current starts at $\theta = 90°$, where B_z changes sign from positive to negative. The most intense current is observed for $\theta = 180°$. The trend is the same for both the weaker and stronger IMF amplitude, but the currents are more intense for the stronger IMF amplitude. For a dominant B_y ($\phi = \pm 90°$), the trend is otherwise the same as for B_x, except that the clear increase starts already at $\theta = 67.5°$ while B_z is still positive. For $\theta > 90°$, the B_x-dominant radial IMF ($\phi = 0°$ or 180°) and the most common Parker spiral IMF ($\phi = -45°$ or 135°) appear to have slightly weaker currents than the B_y-dominant IMF ($\phi = \pm 90°$) or the relatively rare $\phi = 45°$ or $\phi = -135°$ orientations.

Figures 9c and 9d show the Northern Hemisphere cross-polar cap potential, CPCP. Unlike the field-aligned current, which stays more or less constant for $\theta < 67.5°$, CPCP appears to increase as θ increases. The IMF amplitude does not affect CPCP for purely northward IMF orientation. The reason for this could be that CPCP tends to represent the two-cell convection pattern (this can be seen from the locations of the minimum and maximum of the potential, not shown here). However, the IMF amplitude clearly enhances CPCP for $\theta \geq 67.5°$. Similar to the field-aligned current, the B_x-dominant IMF orientations tend to have the weakest CPCP values.

4. Discussion

4.1. Combining the Two Data Sets

Although both the CHAMP and SuperDARN data sets cover the same years 2000–2010, the magnetic field and flow measurements were not obtained from the same locations at the same times. CHAMP provided data more or less continuously, but could only measure at one point at a time, and spent a part of the time outside of the high-latitude regions. SuperDARN measurements, on the other hand, often covered a large part of the high-latitude regions simultaneously, but variations in the occurrence of backscatter, upon which all SuperDARN data products depend, could potentially bias the statistics.

The number of observations by SuperDARN depends on the number of operational radars and the phase of the solar cycle, more observations being seen during solar maximum conditions. Increase in soft-particle precipitation on the dayside and the reconnection electric field that occurs when IMF B_z is strongly negative, as is the case during storms, significantly increase the backscatter. Strong electric fields are also typical on the nightside during storms and increase the backscatter. However, there can be a loss or reduction of backscatter in regions of energetic particle precipitation and after a long exposure to strong electric fields, typically occurring at substorm onset, due to absorption of radio waves by the enhanced electron densities or rapid changes in radio wave propagation conditions [*Wild and Grocott*, 2008; *Gillies et al.*, 2011].

When there is no backscatter from a certain region, the data set we have used does not specify whether this is because of very quiet conditions (no backscatter), very active conditions (loss or reduction of backscatter),

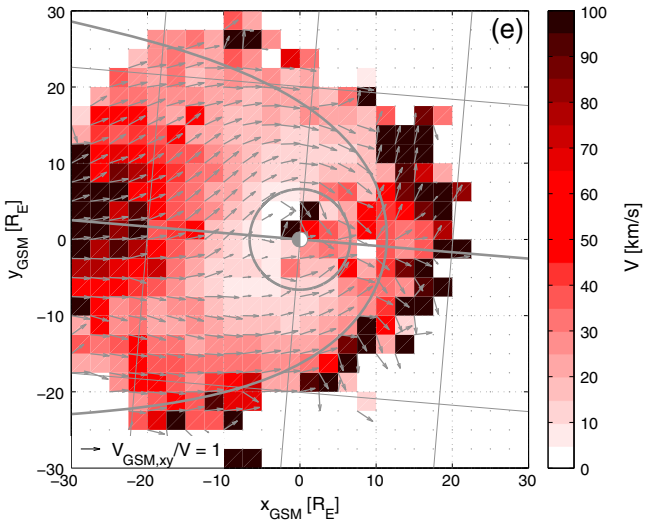

Figure 10. Mean plasma sheet flow speed (color) and direction (vectors) projected onto the GSM *xy* plane. The lengths of the velocity vectors have been normalized to unity, and the *xy* component is displayed. The gray circle represents the geostationary orbit at the 6.6 R_E radial distance, and the gray curve the magnetopause according to *Shue et al.* [1997], with $P_{dyn} = 1$ nPa and IMF $B_z = 0$. Both the magnetopause and the solid grid have been rotated 4.8° clockwise to take into account the aberration due to Earth's orbital motion. The thick gray line shows the aberrated noon-midnight axis. The Figure is reproduced from *Juusola et al.* [2011].

or missing data (radar not operational). As a result, the missing zeros could cause the mean convection for quiet times to come out as too active in some regions, whereas the missing active periods could cause the mean convection for active times to come out as too quiet in some regions. This could affect not just the amplitude but also the direction of the flows. This bias is not expected to be a problem for the results presented here, but any further studies where substorm onset times may play a role must be approached with caution.

4.2. Comparison With Existing Field-Aligned Current Models

He et al. [2012] used the same CHAMP data set as we have to produce a high-resolution model of field-aligned currents parameterized by IMF clock angle, IMF component in the *y-z* plane, IMF magnitude, solar wind speed, and the *AE* index. The model did not cover the whole polar cap: mainly the Region 1 and Region 2 currents were reproduced, while parts of the NBZ currents were not covered.

The maximum current density in the model ranges from about 0.5 to 2 A/km^2, which was noted to be more intense than previous models and close to that observed for individual events. The Region 1 peak spans 2–3° in latitude, which was also noted to be typical for observations. Our Region 1 can be as thin as 2–4° in latitude but is often considerably wider particularly on the nightside. Our maximum current densities are comparable to those of the *He et al.* [2012] model, ranging from 0.5 to 1.9 A/km^2, and our NBZ amplitudes (Figures 5a and 7a) are in agreement with those of *Stauning* [2002]. The hemispherical integrated FAC in our models varies from $(3.2 \pm 0.7)/2 = 1.6 \pm 0.4$ to $(16.7 \pm 2.7)/2 = 8.4 \pm 1.4$ MA, which is in agreement with or higher than existing models [e.g., *He et al.*, 2012].

In the model of *He et al.* [2012], the downward and upward currents maximize typically in the prenoon and postnoon sectors, respectively, which is expected for a current system consisting mainly of Region 1 and Region 2. In our models, the strongest current density is typically attributed to Region 0 when IMF has a northward component and to Region 1 when IMF has a southward component. In agreement with *Weimer* [2001], *Papitashvili et al.* [2002], *Anderson et al.* [2008], and *He et al.* [2012], for IMF $B_y > 0$ ($B_y < 0$) our models show (Figures 5p, 7p, 5n, and 7n) that the dawnside (duskside) Region 1 current sheet appears to cross the noon meridian and extend into the duskside (dawnside) Region 2.

4.3. Mapping to the Magnetosphere

Under steady conditions and in the absence of parallel electric fields, ionospheric convection would be a direct map of plasma and magnetic flux convection in the magnetosphere [*Hesse et al.*, 1997]. Although these conditions are rarely, if ever, quite valid, comparison of the ionospheric and magnetospheric

convection patterns on the one hand, and of the ionospheric convection and field-aligned current patterns on the other hand, can provide us with information on where the field-aligned currents map in the magnetosphere.

Figure 10, reproduced from *Juusola et al.* [2011], shows the statistical direction (arrows) and amplitude (color) of earthward plasma sheet flows in the equatorial plane, determined from 15 years of Cluster, Geotail, and THEMIS satellite data. The plasma sheet pattern shows that earthward flows tend to deviate duskward and dawnward already quite far from Earth such that the majority of the flows actually reach the dayside without having traveled through the nightside near-Earth region. This same tendency can also be seen in the ionospheric flow pattern in Figure 3c (no IMF filtering has been applied to the distributions in Figures 2 and 3. Thus, the conditions for them are the same as for Figure 10): the antisunward flows approaching the nightside oval deviate duskward between about 18 MLT and midnight and dawnward between midnight and about 03 MLT. A preference for the duskward direction can be seen both in the plasma sheet (Figure 10) and in the nightside ionosphere (Figure 3c). As they approach Earth, the earthward plasma sheet flows slow down [*Angelopoulos et al.*, 1994]. Thus, there is a region of almost stagnant flow in the nightside inner magnetosphere in Figure 10. This could correspond to the small flow speeds in the equatorward part of the nightside auroral oval in Figure 3c. Analogous to the nightside, on the dayside the majority of the ionospheric flows do not pass through noon before turning antisunward again. Instead, the change of direction happens in a wide MLT sector extending from about 07 to 17. This would correspond to flows in the plasma sheet not needing to pass through the subsolar point but reconnection being possible along a large MLT sector of the magnetopause.

5. Conclusions

We have used over 10 years of magnetic field data from the CHAMP satellite to construct a set of novel models of the high-latitude ionospheric horizontal and field-aligned current distribution at the spatial resolution of $2° \times 2°$. Because of the technique used to construct the models (SECS), the magnetic field signature due to the current distribution can be directly extracted at any location, such as on the ground or at any low-orbit satellite altitude. This method facilitates a simulation of the magnetic field signature seen by a satellite crossing at a certain magnetic local time, for instance, or by a ground-based magnetometer as it revolves under the pattern, including any derived products, such as some high-latitude magnetic indices (e.g., *AL* and limited local time equivalents).

The current distribution models were complemented by a corresponding set of ionospheric convection models, derived from SuperDARN data measured during the same period as CHAMP data. Both sets of models were similarly parameterized and resolved at the same spatial grid. Combining the current distributions with the electric field extracted from the convection model can provide a way for estimating the Hall and Pedersen conductances and currents as well as Joule heating. This, however, will be a topic for a future study. In this study we have shown that both independent data sets are able to produce the expected distributions, the details of which are in agreement with each other.

We have shown combined distributions of the ionospheric high-latitude field-aligned current and convection extracted from a set of the models parameterized by the orientation and amplitude of the IMF. Our main results are as follows:

1. During purely southward IMF, the ionospheric convection follows a two-cell configuration with associated Region 1 and Region 2 field-aligned current systems. This is consistent with subsolar magnetopause reconnection.
2. During purely northward IMF, the two-cell pattern with associated Region 1 and 2 currents is weak. Superposed on it on the dayside, there is a reversed two-cell convection pattern with associated Region 0 and enhanced Region 1 field-aligned currents. This is consistent with lobe reconnection.
3. For a nonzero IMF B_x, the sign of B_z determines whether there will be lobe ($B_z > 0$) or subsolar reconnection ($B_z < 0$) signatures. However, the presence of B_x will weaken the signatures such that the stronger B_x is compared to B_z the weaker the signatures will be compared to pure northward or southward IMF.
4. When the IMF rotates from pure northward to duskward or dawnward, the distinct reversed and forward two-cell patterns start to merge into a distorted two-cell pattern. This is in agreement with a nonzero IMF B_y displacing the reconnection location from the open field lines to closed dawn or dusk field lines,

even though IMF B_z remains positive. As the IMF continues to rotate southward, the distorted pattern transforms smoothly to that of the symmetric two-cell pattern.

5. While the IMF direction determines the configuration of the field-aligned current density and convection, the IMF amplitude affects their intensity such that a weaker IMF produces weaker field-aligned currents and flows, and a stronger IMF produces stronger current and flows.

Acknowledgments

We thank A. Viljanen for valuable discussions and P. Ritter for providing the CHAMP data. The CHAMP mission is sponsored by the Space Agency of the German Aerospace Center (DLR) through funds of the Federal Ministry of Economics and Technology, following a decision of the German Federal Parliament (grant code 50EE0944). The data retrieval and operation of the CHAMP satellite by the German Space Operations Center (GSOC) of DLR is acknowledged. The SuperDARN data used in this study were processed as part of the European Cluster Assimilation Technology (ECLAT) project. The research leading to these results has received funding from the European Union Seventh Framework Programme (FP7/2007-2013) under grant agreement 263325. We acknowledge NASA/GSFC's Space Physics Data Facility's OMNIWeb service, and OMNI data. The work of L. Juusola was supported by the Academy of Finland project 137900, S. E. Milan and M. Lester by STFC grant ST/K001000/1, A. Grocott by NERC grant NE/G019665/1, and S. M. Imber by ECLAT. We acknowledge the financial support by the Academy of Finland to the ReSoLVE Center of Excellence (project 272157).

Robert Lysak thanks Stephan Buchert and Gareth Chisham for their assistance in evaluating this paper.

References

Amm, O. (1997), Ionospheric elementary current systems in spherical coordinates and their application, *J. Geomagn. Geoelectr.*, *49*, 947–955.

Amm, O., and A. Viljanen (1999), Ionospheric disturbance magnetic field continuation from the ground to ionosphere using spherical elementary current systems, *Earth Planets Space*, *51*, 431–440.

Anderson, B. J., H. Korth, C. L. Waters, D. L. Green, and P. Stauning (2008), Statistical Birkeland current distributions from magnetic field observations by the Iridium constellation, *Ann. Geophys.*, *26*(3), 671–687.

Angelopoulos, V., C. Kennel, F. Coroniti, R. Pellat, M. Kivelson, R. Walker, C. Russell, W. Baumjohann, W. Feldman, and J. Gosling (1994), Statistical characteristics of bursty bulk flow events, *J. Geophys. Res.*, *99*(A11), 21,257–21,280.

Axford, W. I., and C. O. Hines (1961), A unifying theory of high-latitude geophysical phenomena and geomagnetic storms, *Can. J. Phys.*, *39*, 1433–1464.

Baker, K. B., and S. Wing (1989), A new magnetic coordinate system for conjugate studies at high latitudes, *J. Geophys. Res.*, *94*(A7), 9139–9143, doi:10.1029/JA094iA07p09139.

Chisham, G., et al. (2007), A decade of the Super Dual Auroral Radar Network (SuperDARN): Scientific achievements, new techniques and future directions, *Surv. Geophys.*, *28*, 33–109, doi:10.1007/s10712-007-9017-8.

Chisham, G., M. P. Freeman, G. A. Abel, W. A. Bristow, A. Marchaudon, J. M. Ruohoniemi, and G. J. Sofko (2009), Spatial distribution of average vorticity in the high-latitude ionosphere and its variation with interplanetary magnetic field direction and season, *J. Geophys. Res.*, *114*, A09301, doi:10.1029/2009JA014263.

Dungey, J. W. (1961), Interplanetary magnetic field and the auroral zones, *Phys. Rev. Lett.*, *6*, 47–48.

Dungey, J. W. (1963), The structure of the ionosphere, or adventures in velocity space, in *Geophysics: The Earth's Environment*, edited by C. DeWitt, J. Hiebolt, and A. Lebeau, pp. 526–536, Gordon and Breach, New York.

Fukushima, N. (1976), Generalized theorem for no ground magnetic effect of vertical currents connected with Pedersen currents in the uniform-conductivity ionosphere, *Rep. Ionos. Space Res. Japan*, *30*, 35–40.

Gillies, D. M., K. A. McWilliams, J.-P. S. Maurice, and S. E. Milan (2011), Global-scale observations of ionospheric convection during geomagnetic storms, *J. Geophys. Res.*, *116*, A12238, doi:10.1029/2011JA017086.

Greenwald, R. A., et al. (1995), Darn/Superdarn: A global view of the dynamics of high-latitude convection, *Space Sci. Rev.*, *71*(1–4), 761–796.

He, M., J. Vogt, H. Lühr, E. Sorbalo, A. Blagau, G. Le, and G. Lu (2012), A high-resolution model of field-aligned currents through empirical orthogonal functions analysis (MFACE), *Geophys. Res. Lett.*, *39*, L18105, doi:10.1029/2012GL053168.

Hesse, M., J. Birn, and R. Hoffman (1997), On the mapping of ionospheric convection into the magnetosphere, *J. Geophys. Res.*, *102*(A5), 9543–9551.

Iijima, T., and T. A. Potemra (1976), The amplitude distribution of field-aligned currents at northern high latitudes observed by Triad, *J. Geophys. Res.*, *81*(13), 2165–2174.

Imber, S. M., S. E. Milan, and B. Hubert (2006), The auroral and ionospheric flow signatures of dual lobe reconnection, *Ann. Geophys.*, *24*, 3115–3129, doi:10.5194/angeo-24-3115-2006.

Imber, S. M., S. E. Milan, and B. Hubert (2007), Observations of significant flux closure by dual lobe reconnection, *Ann. Geophys.*, *25*, 1617–1627, doi:10.5194/angeo-25-1617-2007.

Juusola, L., O. Amm, and A. Viljanen (2006), One-dimensional spherical elementary current systems and their use for determining ionospheric currents from satellite measurements, *Earth, Planets and Space*, *58*, 667–678.

Juusola, L., K. Kauristie, O. Amm, and P. Ritter (2009), Statistical dependence of auroral ionospheric currents on solar wind and geomagnetic parameters from 5 years of CHAMP satellite data, *Ann. Geophys.*, *27*(3), 1005–1017.

Juusola, L., N. Østgaard, and E. Tanskanen (2011), Statistics of plasma sheet convection, *J. Geophys. Res.*, *116*, A08201, doi:10.1029/2011JA016479.

Kamide, Y., P. D. Perreault, S.-I. Akasofu, and J. D. Winningham (1977), Dependence of substorm occurrence probability on the interplanetary magnetic field and on the size of the auroral oval, *J. Geophys. Res.*, *82*(35), 5521–5528.

Luhmann, J. G., R. J. Walker, C. T. Russell, N. U. Crooker, J. R. Spreiter, and S. S. Stahara (1984), Patterns of potential magnetic field merging sites on the dayside magnetopause, *J. Geophys. Res.*, *89*(A3), 1739–1742.

Maus, S., M. Rother, C. Stolle, W. Mai, S. Choi, H. Lühr, D. Cooke, and C. Roth (2006), Third generation of the Potsdam Magnetic Model of the Earth (POMME), *Geochem. Geophys. Geosyst.*, *7*, Q07008, doi:10.1029/2006GC001269.

Milan, S. E. (2004), Dayside and nightside contributions to the cross polar cap potential: Placing an upper limit on a viscous-like interaction, *Ann. Geophys.*, *22*, 3771–3777, doi:10.5194/angeo-22-3771-2004.

Milan, S. E., M. Lester, S. W. H. Cowley, and M. Brittnacher (2000), Dayside convection and auroral morphology during an interval of northward interplanetary magnetic field, *Ann. Geophys.*, *18*, 436–444, doi:10.1007/s00585-000-0436-9.

Milan, S. E., T. A. Evans, and B. Hubert (2010), Average auroral configuration parameterized by geomagnetic activity and solar wind conditions, *Ann. Geophys.*, *28*(4), 1003–1012, doi:10.5194/angeo-28-1003-2010.

Papitashvili, V. O., F. Christiansen, and T. Neubert (2002), A new model of field-aligned currents derived from high-precision satellite magnetic field data, *Geophys. Res. Lett.*, *29*(14), 1683, doi:10.1029/2001GL014207.

Ritter, P., H. Lühr, A. Viljanen, O. Amm, A. Pulkkinen, and I. Sillanpää (2004), Ionospheric currents estimated simultaneously from CHAMP satellite and IMAGE ground-based magnetic field measurements: A statistical study at auroral latitudes, *Ann. Geophys.*, *22*(2), 417–430.

Ruohoniemi, J. M., and K. B. Baker (1998), Large-scale imaging of high-latitude convection with super dual auroral radar network hf radar observations, *J. Geophys. Res.*, *103*(A9), 20,797–20,811, doi:10.1029/98JA01288.

Russell, C. T. (1972), The configuration of the magnetosphere, in *Critical Problems of Magnetospheric Physics*, edited by E. R. Dyer, pp. 1–16, IUCSTP Secretariat, Washington, D. C.

Shue, J.-H., J. K. Chao, H. C. Fu, C. T. Russell, P. Song, K. K. Khurana, and H. J. Singer (1997), A new functional form to study the solar wind control of the magnetopause size and shape, *J. Geophys. Res.*, *102*, 9497–9511.

Stauning, P. (2002), Field-aligned ionospheric current systems observed from Magsat and Oersted satellites during northward IMF, *Geophys. Res. Lett.*, *29*(15), 8005, doi:10.1029/2001GL013961.

Untiedt, J., and W. Baumjohann (1993), Studies of polar current systems using the IMS Scandinavian magnetometer array, *Space Sci. Rev.*, *63*, 245–390.

Weimer, D. R. (1995), Models of high-latitude electric potentials derived with a least error fit of spherical harmonic coefficients, *J. Geophys. Res.*, *100*(A10), 19,595–19,607, doi:10.1029/95JA01755.

Weimer, D. R. (1996), A flexible, IMF dependent model of high-latitude electric potentials having "space weather" applications, *Geophys. Res. Lett.*, *23*(18), 2549–2552.

Weimer, D. R. (2001), Maps of ionospheric field-aligned currents as a function of the interplanetary magnetic field derived from Dynamics Explorer 2 data, *J. Geophys. Res.*, *106*(A7), 12,889–12,902.

Weimer, D. R., D. M. Ober, N. C. Maynard, M. R. Collier, D. J. McComas, N. F. Ness, C. W. Smith, and J. Watermann (2003), Predicting interplanetary magnetic field (IMF) propagation delay times using the minimum variance technique, *J. Geophys. Res.*, *108*(A1), 1026, doi:10.1029/2002JA009405.

Wild, J. A., and A. Grocott (2008), The influence of magnetospheric substorms on SuperDARN radar backscatter, *J. Geophys. Res.*, *113*, A04308, doi:10.1029/2007JA012910.